Estimate of the detectability of the circular polarization signature of supernova gravitational waves using the Stokes parameters

Man Leong Chan and Kazuhiro Hayama
Department of Applied Physics, Fukuoka University, Nanakuma 8-19-1, Fukuoka 814-0180, Japan

(Received 5 August 2020; accepted 5 May 2021; published 28 May 2021)

The circular polarization of gravitational waves from core collapse supernovae has been proposed as a probe to investigate the rotation and physical features inside the core of the supernovae. However, it is still unclear as to how detectable the circular polarization of gravitational waves will be. We developed an algorithm referred to as the Stokes Circular Polarization algorithm for the computation of the Stokes parameters that works with the burst search pipeline coherent WaveBurst. Employing the waveform SFHx and the algorithm, we estimate the detectability of the circular polarization signatures (V mode of the Stokes parameters) for sources across the sky at three different distances 2, 5, and 10 kpc, for a network of gravitational wave detectors consisted of Advanced LIGO, Advanced VIRGO, and KAGRA. Using the Bayes factor, we found that, for 2 and 5 kpc, the majority of the sources (99.9% and 58.2%, respectively) will have their V mode detectable, while, for 10 kpc, no significant V mode is detectable. In addition, the significance of the V mode signature is consistent with the recoverability of the two polarizations of gravitational waves with respect to the network.

DOI: 10.1103/PhysRevD.103.103024

I. INTRODUCTION

Gravitational wave (GW) astronomy has been rapidly developing since the first direct detections from the O1 and O2 observations of LIGO and VIRGO [1–8]. As the sensitivities of the interferometric GW detectors improve, more detections of transient GW events are anticipated [9]. Although at present all the detections have originated from compact binary coalescences, core collapse supernovae (CCSNe) are among the sources of GWs expected to be observable with the second-generation detectors such as Advanced LIGO (aLIGO), Advanced VIRGO (AdVirgo), and KAGRA [10–14].

As a massive star (10–100 $M_\odot$ at zero-age main sequence) reaches the final stage of its stellar life, core collapse is expected to ensue if the mass of the core is larger than the effective Chandrasekhar mass [15,16]. The core collapse will continue until its density is comparable to that of nuclear matter. The inner core will bounce back as the nuclear equation of state stiffens by the strong nuclear force. A shock wave will then be formed and sent through the in-falling matter. By losing energy to the dissociation of the iron nuclei and to neutrino cooling, the shock wave will stall, which will somehow have to be revived if the star is to become a supernova [17]. Although this scenario is supported by the observations of the CCSN SN1987A [18] in 1987, how exactly the shock wave is revived is still unclear to astronomers and has remained the subject of intense study for decades [19].

Currently, two most popular theories, the neutrino-driven mechanism [16,20] and the magnetorotational mechanism, for reviving the shock wave in the inner core, have been put forward. For stars with rapid core spin and a strong magnetic field, the magnetorotational mechanism may be the active mechanism [21–25] (such a requirement may not be absolutely necessary; see, e.g., [26]). The magnetic field and the core spin together may produce an outflow that could possibly cause some of the most energetic CCSNe observed and may be able to explain the extreme hypernovae and the observed long gamma-ray bursts [27–30]. On the other hand, the neutrino-driven mechanism [16,20] theorizes that the revival of the shock wave is achieved by ~5% of the outgoing neutrino energy stored below the shock, which causes turbulence and increases thermal pressure. Convection and the standing accretion shock instability (SASI) [31], observed in supernova simulations, may also be required to produce a CCSN via the neutrino mechanism.

Related to the mechanisms, one important property of massive stars is their rotation profiles, such as the rate of the rotation and the differential rotation. Rotation itself is also a parameter important to the chemical yields and stellar evolution as well as the final stage of its life [32]. However, although stars are generally known to be rotators [33], the rates at which the cores of stars rotate just prior to collapse are still unknown. In part, the rotation of the core of a star may depend on the presence of the magnetic braking of the rotation. It is estimated that periods of a few

seconds are possible if the braking is not present, while the periods can be up to 10 times longer with the presence of angular momentum transfer via magnetic fields [34].

Methods for investigating the rotation of the cores have been proposed in the literature. For example, a signature of the angular momentum distribution was once suggested to be imprinted in the sign of the second-largest peak in the GWs emitted after core bounce [35]. In addition, Abdikamalov *et al.* [36] proposed the use of a waveform template bank for signals from sources with rapid rotations, as well as Bayesian model selection [36]. In recent years, the circular polarization of GWs has been proposed as a probe to investigate the rotation of the core prior to collapse [37,38]. It was pointed out that rapidly rotating cores of massive stars can cause the formation of accretion flows that have a nonaxisymmetric, spiral pattern in the post-shock (for example, see, e.g., [39,40]). The core rotation might also reflect itself as a signature of circular polarization in the emitted GWs at a frequency twice that of the rotation [37].

However, galactic supernovae are predicted to occur at a single-digit rate per century by most studies. For example, van den Bergh and Tammann [41] and Cappellaro *et al.* [42] derived a rate of 1.7 ± 0.9 and 3.4 ± 2.0 per century, respectively. More recently, a rate of 1.0–2.0 per century was estimated in Ref. [43]. Since the majority of supernova progenitors are believed to have rotations too slow to have an important role in the dynamics [44–46], rapidly rotating supernovae are believed to occur at an even rarer rate and account for only a small fraction of galactic supernova events.

While it is true that rapidly rotating supernova progenitors may be rare, the circular polarization of a GW may also help understand the physical features deep in the core of a non- or slowly rotating supernova such as the proto-neutron-star oscillation and SASI activity, which are the characteristic features of their GWs. For instance, it has been recognized that the circular polarization signature of the GWs from CCSNe may contain information on the spiral mode of the SASI activity [38,47] and the ramp-up g mode of the proto-neutron-star oscillation and can, therefore, be used as a probe of these features. One such example is the SFHx waveform in Ref. [48]. The circular polarization of GWs may also show the evolution of the asymmetry between the right-handed and left-handed mode (defined in Sec. II) over time and frequency [38].

However, the detection of a GW signal depends on the combined antenna pattern of GW detectors to the source location, while the recoverability of the circular polarization signature of a GW relies on both the sensitivities of the GW detectors to the two polarizations of the signal. Therefore, one question that can be asked is, will we be able to recover the circular polarization signatures of the GWs from CCSNe if such signals are detected? In Ref. [38], the authors tried to answer such a question. The answer turned out to be positive. The analysis, however, was based on only one example. This means that the conclusion itself may not be entirely representative.

In this work, we extend the method and the work presented in Refs. [37,38] and develop an algorithm that computes the Stokes parameters in the time-frequency domain. The algorithm works with the detection pipeline coherent WaveBurst (cWB) [49], which is one of the main detection pipelines employed in LIGO and VIRGO and was among the first pipelines to achieve the first direct detection of GWs [50]. Using the simulated waveform SFHx from Ref. [48] as an example and the developed algorithm, we try to answer the question in a more general manner by performing simulations of sources across the sky. This paper is structured as follows: In Sec. II, we will present a brief explanation of the Stokes parameters. Section III will then be devoted to the algorithm developed for the computation of the parameters. In Sec. IV, the details of the simulations are given. The results and a discussion are presented in Sec. V, which is followed by a conclusion in Sec. VI.

II. THE STOKES PARAMETERS

The Stokes parameters [40] are a set of physical values that can be used to describe the polarization status of GWs [51]. The mathematical definition of the Stokes parameters is given by

$$\begin{aligned}
\langle \tilde{h}_R(f,\hat{n})\tilde{h}_R(f',\hat{n}')^*\rangle &= \frac{1}{4\pi}\delta_D^2(\hat{n}-\hat{n}')\delta_D^2(f-f') \\
&\quad \times (I(f,f',\hat{n},\hat{n}')+V(f,f',\hat{n},\hat{n}'));\\
\langle \tilde{h}_L(f,\hat{n})\tilde{h}_R(f',\hat{n}')^*\rangle &= \frac{1}{4\pi}\delta_D^2(\hat{n}-\hat{n}')\delta_D^2(f-f') \\
&\quad \times (Q(f,f',\hat{n},\hat{n}')-iU(f,f',\hat{n},\hat{n}'));\\
\langle \tilde{h}_R(f,\hat{n})\tilde{h}_L(f',\hat{n}')^*\rangle &= \frac{1}{4\pi}\delta_D^2(\hat{n}-\hat{n}')\delta_D^2(f-f') \\
&\quad \times Q(f,f',\hat{n},\hat{n}')+iU(f,f',\hat{n},\hat{n}'));\\
\langle \tilde{h}_L(f,\hat{n})\tilde{h}_L(f',\hat{n}')^*\rangle &= \frac{1}{4\pi}\delta_D^2(\hat{n}-\hat{n}')\delta_D^2(f-f') \\
&\quad \times I(f,f',\hat{n},\hat{n}')-V(f,f',\hat{n},\hat{n}'));
\end{aligned} \tag{1}$$

where f is the frequency, $\hat{n}$ is the unit vector in the propagation direction, and $\langle\rangle$ represents the ensemble average. In terms of GW observations, since in reality there is only one observation at a time, the ensemble average is just the time series itself. The tilde on top of a symbol represents Fourier transform. In the above equation, $\tilde{h}_R$ and $\tilde{h}_L$ are the right-handed and left-handed mode of GW, respectively, as given by

$$\tilde{h}_R(f,\hat{n}) \equiv \frac{(\tilde{h}_+(f,\hat{n}) - \mathrm{i}\tilde{h}_\times(f,\hat{n}))}{\sqrt{2}},$$
$$\tilde{h}_L(f,\hat{n}) \equiv \frac{(\tilde{h}_+(f,\hat{n}) + \mathrm{i}\tilde{h}_\times(f,\hat{n}))}{\sqrt{2}}, \quad (2)$$

where the terms $\tilde{h}_+$ and $\tilde{h}_\times$ are the two polarizations of GW. I, Q, U, and V are the full set of the Stokes parameters. They describe different properties of a GW. For instance, the parameter I represents the total amplitudes of the right-handed and left-handed mode, and Q and U the linear polarization status. In particular, the parameter V describes the circular polarization. Since we are interested in the circular polarization of GWs, we will focus on the V parameter, which we will refer to as the V mode in this paper. With some algebraic manipulations, it can be shown from Eq. (1) that the V mode can be written as

$$\delta_D^2(\hat{n}-\hat{n}')\delta_D^2(f-f')V = 2\pi\langle\tilde{h}_R(f,\hat{n})\tilde{h}_R(f',\hat{n}')^*\rangle - \langle\tilde{h}_L(f,\hat{n})\tilde{h}_L(f',\hat{n}')^*\rangle; \quad (3)$$

in other words, the V mode also describes the amplitude asymmetries between the right-handed and left-handed mode.

III. ALGORITHM

As mentioned in the introduction, we develop an algorithm for the computation of the V mode of GWs in the time-frequency domain. The algorithm is illustrated in Fig. 1. For the remainder of this paper, the algorithm will be referred to as the Stokes circular polarization (SCP) algorithm. As shown in the flow chart, if a trigger is identified by cWB and the SCP algorithm is called, it will first input the corresponding whitened time series from all the detectors in the network at time t from cWB as $\mathbf{d}(t)$, given by

$$\mathbf{d}(t) = \mathbf{F}_+ h_+(t) + \mathbf{F}_\times h_\times(t), \quad (4)$$

where the components of the matrices $\mathbf{F}_+$ and $\mathbf{F}_\times$ denote the antenna pattern of each detector. Since the V mode describes the asymmetry of the right-handed and left-handed mode of a GW, which are related to the two polarizations h_+ and $h_\times$ by Eqs. (2) and (3), the first step is to recover h_+ and $h_\times$ from $\mathbf{d}$. This is achieved in the SCP algorithm by using the following equations [52]:

$$h_+^r(t) = \frac{(\mathbf{F}_+\cdot\mathbf{d}(\mathbf{t}))(|\mathbf{F}_\times|^2) - (\mathbf{F}_\times\cdot\mathbf{d}(\mathbf{t}))(\mathbf{F}_+\cdot\mathbf{F}_\times)}{|\mathbf{F}_+|^2|\mathbf{F}_\times|^2 - (\mathbf{F}_+\cdot\mathbf{F}_\times)^2},$$
$$h_\times^r(t) = \frac{(\mathbf{F}_\times\cdot\mathbf{d}(\mathbf{t}))(|\mathbf{F}_+|^2) - (\mathbf{F}_+\cdot\mathbf{d}(\mathbf{t}))(\mathbf{F}_+\cdot\mathbf{F}_\times)}{|\mathbf{F}_+|^2|\mathbf{F}_\times|^2 - (\mathbf{F}_+\cdot\mathbf{F}_\times)^2}, \quad (5)$$

where $h_+^r(t)$ and $h_\times^r(t)$ are the reconstructed polarization components and the superscript r stands for reconstruction. To use Eqs. (5), the SCP algorithm can employ the estimates either of the sky location and the arrival time of the signal from the cWB or from electromagnetic and/or neutrino observations in situations where they are available. The next step is to reconstruct the V mode of the signal using $h_+^r(t)$ and $h_\times^r(t)$, which will be explained in Sec. III A.

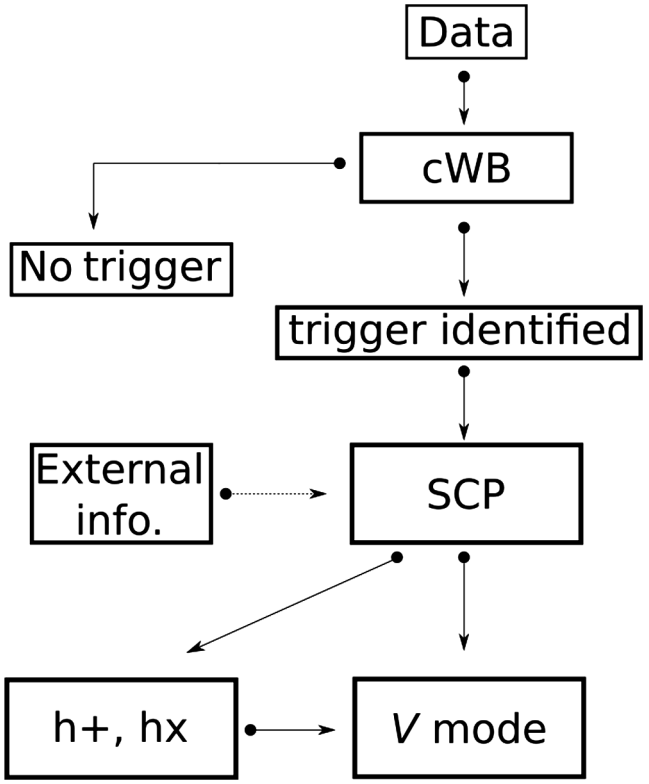

FIG. 1. An flow chart showing the work flow of the algorithm for the V mode computation. It works by first extracting the whitened time series from the pipeline cWB if there is a trigger identified by the pipeline. Using either the estimates on the arrival time of the event and the sky location from the cWB or external information such as that from electromagnetic observations or neutrino observations, the algorithm will then recover the two polarizations h_+ and $h_\times$. From the two polarizations, the algorithm will then compute the V mode of the trigger. The dashed line connecting external information and SCP indicates that the algorithm may or may not use the information from external sources.

A. Reconstruction of V mode

In the SCP algorithm, the V mode is computed in the time-frequency domain. This is done by applying a window of a preselected length to $h_+^r(t)$ and $h_\times^r(t)$, denoted by $g_+^r(t)$ and $g_\times^r(t)$, respectively. The segments $g_+^r(t)$ and $g_\times^r(t)$ are then converted to the frequency domain [i.e., $\tilde{g}_+^r(f)$ and $\tilde{g}_\times^r(f)$] by performing Fourier transform. The easiest way to achieve the V mode for these segments is to substitute $\tilde{g}_+^r(f)$ and $\tilde{g}_\times^r(f)$ for $\tilde{h}_+(f)$ and $\tilde{h}_\times(f)$, respectively, in Eq. (2). The V mode can subsequently be computed using Eq. (3). The window is then slid in time by a preselected

amount such that the current windowed segment $g^r_+(t)$ and $g^r_\times(t)$ will be overlapping in time with the previous segment. This procedure is repeated until all segments of $h^r_+(t)$ and $h^r_\times(t)$ are converted to the frequency domain and their corresponding V modes computed. The reconstruction of the V mode for the trigger in the time-frequency domain is achieved by combining all these individual V modes together in order of time, which we denote by $\mathbf{V}_\mathrm{o}$.

However, for a random trigger, $\mathbf{V}_\mathrm{o}$ computed in such a way will not be entirely free of noise. To determine the V mode of a trigger, we further take the following procedure: First, N whitened time series, $\mathbf{d}^\mathrm{n}_k$, of the same duration as the trigger, strictly contiguous and adjacent to the time of the event as estimated by cWB, are taken. The superscript n indicates that these time series contain only noise, and the subscript k ranges from 1 to N. The value N is an arbitrary number chosen before the calculation. We then compute the V mode for each of $\mathbf{d}^\mathrm{n}_k$ by substituting $\mathbf{d}^\mathrm{n}_k$ for $\mathbf{d}$ in Eq. (5), while using the same values of $\mathbf{F}_+$ and $\mathbf{F}_\times$ and the arrival times as those for $\mathbf{V}_\mathrm{o}$. The V modes obtained are denoted by $\mathbf{V}^\mathrm{n}_k$. As $\mathbf{V}^\mathrm{n}_k$ is computed in the time-frequency domain, each $\mathbf{V}^\mathrm{n}_k$ contains m time-frequency pixels, where m is a number depending on the number of overlap and fast Fourier transform window. This means in total there will be $N \times m$ time-frequency pixels.

The final step is then to rank the $N \times m$ pixels based on their absolute values. The value larger than a preselected fraction F_o (e.g., 0.99) of the pixels will be selected as a threshold p_thr. For a pixel from $\mathbf{V}_\mathrm{o}$ to be considered relevant to the trigger rather than random noise, its absolute value has to be larger than p_thr. The collection of the pixels $> p_\mathrm{thr}$ from $\mathbf{V}_\mathrm{o}$ as well as their corresponding time and frequency is then the V mode of the trigger, denoted by $\mathbf{V}_\mathrm{t}$, where the subscript t stands for >threshold.

B. Significance of V mode

Once the $\mathbf{V}_\mathrm{t}$ of a trigger is reconstructed, it is necessary to establish its significance. To do so, we employ the Bayes factor. The Bayes factor is a ratio of the posteriors of two competing models or hypotheses, as defined by the following equation:

$$B_{\mathrm{H}_1/\mathrm{H}_0} = \frac{p(\mathrm{H}_1|\mathbf{d})}{p(\mathrm{H}_0|\mathbf{d})}, \tag{6}$$

where $p(\mathrm{H}_0|\mathbf{d})$ is the posterior of the null hypothesis H_0 given $\mathbf{d}$ and $p(\mathrm{H}_1|\mathbf{d})$ the posterior of the alternative hypothesis given $\mathbf{d}$. The Bayes factor measures how much a hypothesis or a model is favored by the data against another competing hypothesis or model. If the value of $B_{\mathrm{H}_1/\mathrm{H}_0}$ is larger than 1, it means H_1 is favored by the data, or the data are in favor of H_0 if the value is less than 1. While Bayes factors are similar to the signal-to-noise ratio of a signal in the sense that they can both be used to estimate the significance of the presence of a signal, they are not equal.

Since our purpose is to determine the presence or absence of the V mode of a trigger, H_1 is the hypothesis that a V mode signature is present in the data, and H_0 no V mode signature is present in the data. Using the Bayes' theorem and substituting $\mathbf{V}_\mathrm{o}$ for $\mathbf{d}$, Eq. (6) can be written as

$$B_{\mathrm{H}_1/\mathrm{H}_0} = \frac{p(\mathrm{H}_1)}{p(\mathrm{H}_0)} \frac{p(\mathbf{V}_\mathrm{o}|\mathrm{H}_1)}{p(\mathbf{V}_\mathrm{o}|\mathrm{H}_0)}. \tag{7}$$

In the above equation, $p(\mathrm{H}_1)$ and $p(\mathrm{H}_0)$ are the prior probabilities for H_1 and H_0, respectively, which we set to be equal. The term $p(\mathbf{V}_\mathrm{o}|\mathrm{H}_1)$ is the likelihood of $\mathbf{V}_\mathrm{o}$ given H_1 and $p(\mathbf{V}_\mathrm{o}|\mathrm{H}_0)$ the likelihood of $\mathbf{V}_\mathrm{o}$ given H_0. We approximate the likelihood function using a Gaussian distribution, so the joint probability densities can be written as

$$\begin{aligned} p(\mathbf{V}_\mathrm{o}|\mathrm{H}_1) &= \left(\prod_i^m \frac{1}{\sqrt{2\pi}\sigma_i} \exp -\frac{1}{2m} \left(\frac{V_{\mathrm{o}i} - V_{\mathrm{t}i} - V_{\mathrm{M}i}}{\sigma_i} \right)^2 \right)^{1/m} \\ p(\mathbf{V}_\mathrm{o}|\mathrm{H}_0) &= \left(\prod_i^m \frac{1}{\sqrt{2\pi}\sigma_i} \exp -\frac{1}{2m} \left(\frac{V_{\mathrm{o}i} - V_{\mathrm{M}i}}{\sigma_i} \right)^2 \right)^{1/m}, \end{aligned} \tag{8}$$

where $V_{\mathrm{o}i}$, $V_{\mathrm{t}i}$, and $V_{\mathrm{M}i}$ are the ith pixel from $\mathbf{V}_\mathrm{o}$, $\mathbf{V}_\mathrm{t}$, and $\mathbf{V}_\mathrm{M}$, respectively. $\mathbf{V}_\mathrm{M}$ and σ are the mean and standard deviation of $\mathbf{V}^\mathrm{n}_k$, respectively. In addition, we normalize the likelihood functions by taking the geometric mean of the functions over the number of pixels (mth root). This is to prevent artificial change of the value of Bayes factor due to the change of overlaps and the Fourier transform window. Finally, for our analysis, we will use the logarithm of the Bayes factor $\log B_{\mathrm{H}_1/\mathrm{H}_0}$ for the remainder of this paper.

As an example to show how the SCP algorithm works, we test the algorithm against three cases where the signals are sine-Gaussian waves. The sine-Gaussian waves are generated using the following equations:

$$\begin{aligned} h_+(t) &= h \frac{1 + \cos^2(\iota)}{2} \sin(2\pi t f_0) e^{-2\pi^2 f_0^2 t^2/Q^2}, \\ h_\times(t) &= h \cos(\iota) \cos(2\pi t f_0) e^{-2\pi^2 f_0^2 t^2/Q^2}, \end{aligned} \tag{9}$$

where h is the amplitude, Q the quality factor, f_0 the frequency, and ι the inclination angle. For simplicity, we generate three distinct cases with three different values of ι (i.e., 0°, 70°, and 90°, respectively), while keeping the values of $Q = 9$ and $f_0 = 200$ Hz for all three cases. These three values of ι are chosen to represent different polarization status, such as circular polarization ($\iota = 0°$), elliptical polarization ($\iota = 70°$), and linear polarization ($\iota = 90°$), as seen from the observer. For a fair comparison between these three cases, the sky locations of the sources are chosen to be the same at $(\mathrm{longitude}, \mathrm{latitude}) = (-90°, 30°)$, and the values of h are chosen such that each sine-Gaussian wave has the same value of h_rss (i.e., 8.3×10^{-23}). The network consists of aLIGO Hanford,

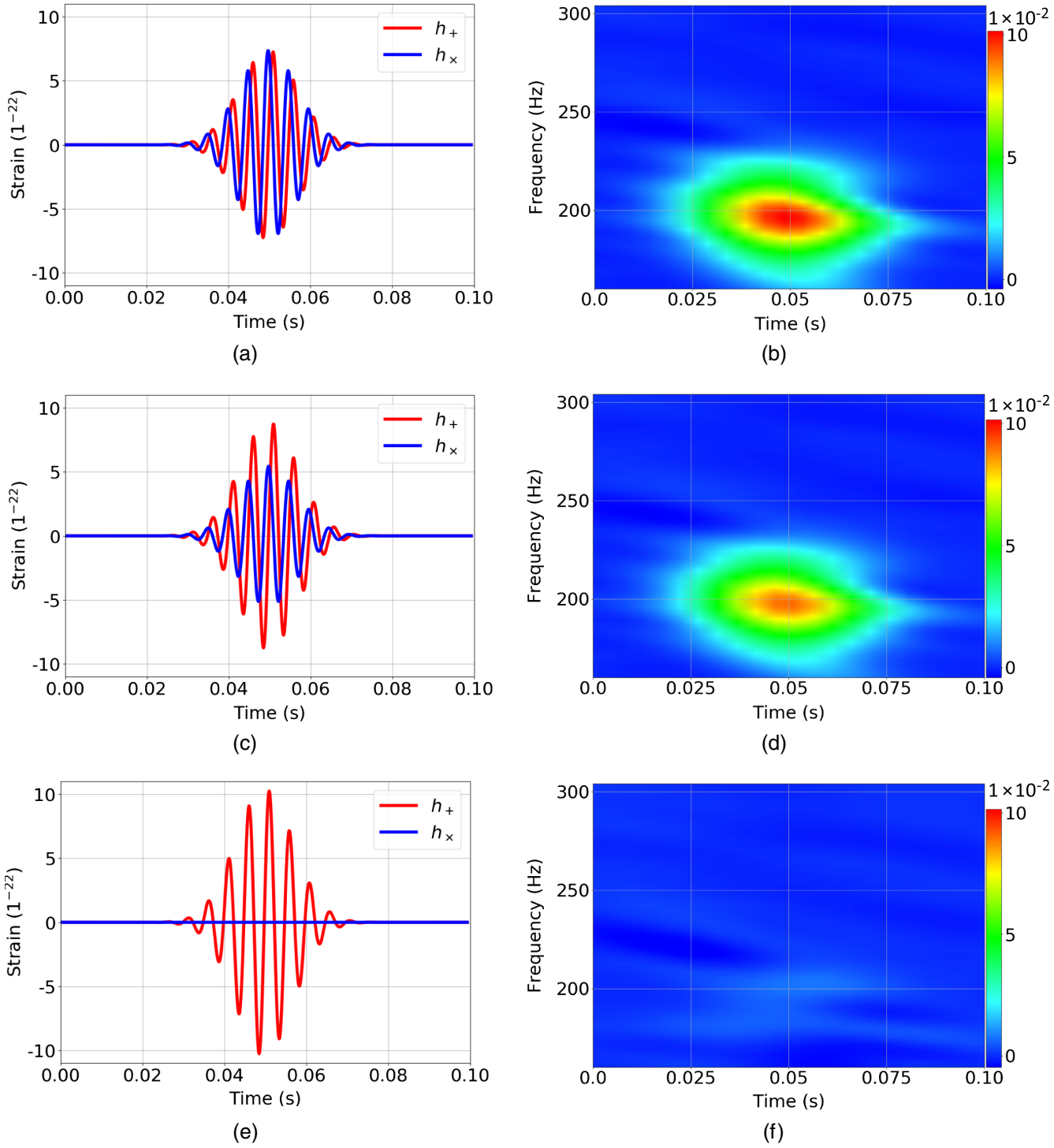

FIG. 2. Examples of sine-Gaussian waveforms and their V mode presented in the time-frequency domain. From the top to the bottom, the left panels show the sine-Gaussian waveforms generated at $\iota = 0°$, $70°$, $90°$, respectively. The amplitudes are normalized to $h_{\rm rss} = 8.3 \times 10^{-23}$. The sources are injected at (longitude, latitude) $= (-90°, 30°)$. The panels on the right show the respective V mode computed using the whitened time series from cWB.

aLIGO Livingston, AdVirgo, and KAGRA. The noise is Gaussian noise generated using the power spectrum densities at their respective design sensitivity [9,11,53]. For the settings in the SCP algorithm, we choose N to be 100 and F_o to be 0.99. The true values of arrival times and the antenna pattern are used. The results are shown in Fig. 2. From $\iota = 0$ to $90°$, a decrease in the magnitude of the V mode can be seen. This indicates that the magnitude of the V mode

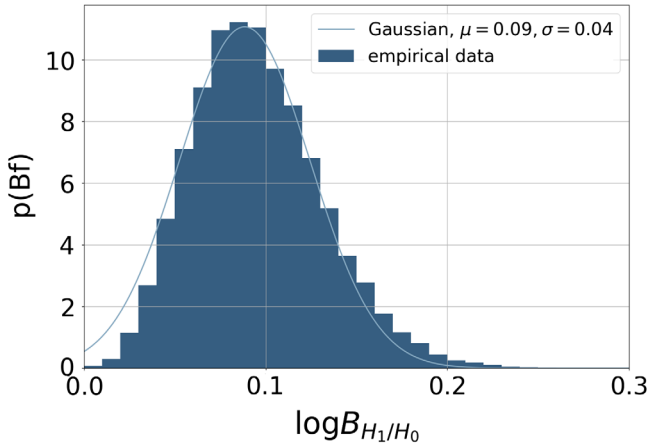

FIG. 3. Histogram showing the distribution of $\log B_{\mathrm{H_1/H_0}}$ where the signals are of zero amplitude and distributed across the sky randomly. The light blue curve shows a Gaussian distribution with mean and standard deviation equal to 0.09 and 0.04, respectively.

captures the extent to which the signal is circularly polarized. For the sine-Gaussian waves at $\iota = 0°$, 70°, 90°, the $\log B_{\mathrm{H_1/H_0}}$ are 67.2, 55.0, and 0.4, respectively. If we consider $\mathrm{H_1}$ is preferred when $\log B_{\mathrm{H_1/H_0}} \geq 8$, then it can be seen that, for the cases at $\iota = 0°$ and 70°, $\mathrm{H_1}$ is preferred, while, for $\iota = 90°$, $\mathrm{H_0}$ is preferred, which are as expected.

To justify the use of $\log B_{\mathrm{H_1/H_0}} \geq 8$ as the criterion based on which the detection of a V mode is determined, we inject 5×10^4 signals with zero amplitudes across the entire sky and employ the SCP algorithm to estimate the significance of their V modes. Since signals with zero amplitudes will not be identified as triggers in cWB, in this simulation, the SCP algorithm is forced to carry out the procedure described in Sec. III. To obtain a more reliable result, we increase the value of N to 2000. Similarly, the true values of the arrival times and the antenna pattern are used. The result is shown in Fig. 3. It can be seen that, compared to a Gaussian distribution with mean and variance equal to 0.09 and 0.04, respectively, the distribution of the values of $\log B_{\mathrm{H_1/H_0}}$ is slightly tilted. Given how $\mathbf{V}_\mathrm{t}$ is defined (see Sec. III A), which is by taking the pixels that are exceeding a threshold, it is impossible for the values of $\log B_{\mathrm{H_1/H_0}}$ to be less than zero. The distribution, as compared to a Gaussian distribution, is therefore truncated at $\log B_{\mathrm{H_1/H_0}} = 0$, and an extra fraction of samples inevitably accumulate on the side larger than 0. Given the distribution shown in Fig. 3, the requirement of $\log B_{\mathrm{H_1/H_0}} \geq 8$ is a conservative one.

The above described approach can suppress most time-frequency pixels irrelevant to a trigger. While this works well for strong signals, we also note that signals with pixels associated with weak amplitudes can potentially be ruled out, especially in situations where prior knowledge on the waveforms of the signals is not available. As an example, we show the $\mathbf{V}_\mathrm{o}$ and $\mathbf{V}_\mathrm{t}$ of a trigger in Fig. 4 where the injected waveform is SFHx (see Sec. IV for details of the waveform) and the source is located at (longitude, latitude) $= (-145°, 70°)$ and 10 kpc from Earth. It can be seen that the peaks of $\mathbf{V}_\mathrm{t}$ occur at times and frequencies that are generally consistent with those shown in Fig. 6, which shows the SFHx waveform and its V mode. However, the amplitudes of the signal are so weak that they do not significantly deviate from noise, resulting in a value of $\log B_{\mathrm{H_1/H_0}}$ equal to 0.4, indicating the difficulty of detecting and reconstructing the V mode of a signal without any prior knowledge on the waveform.

IV. V MODE OBSERVABILITY

As indicated in Eq. (5), if at a location in the sky the value of the denominator on the right-hand side is close to

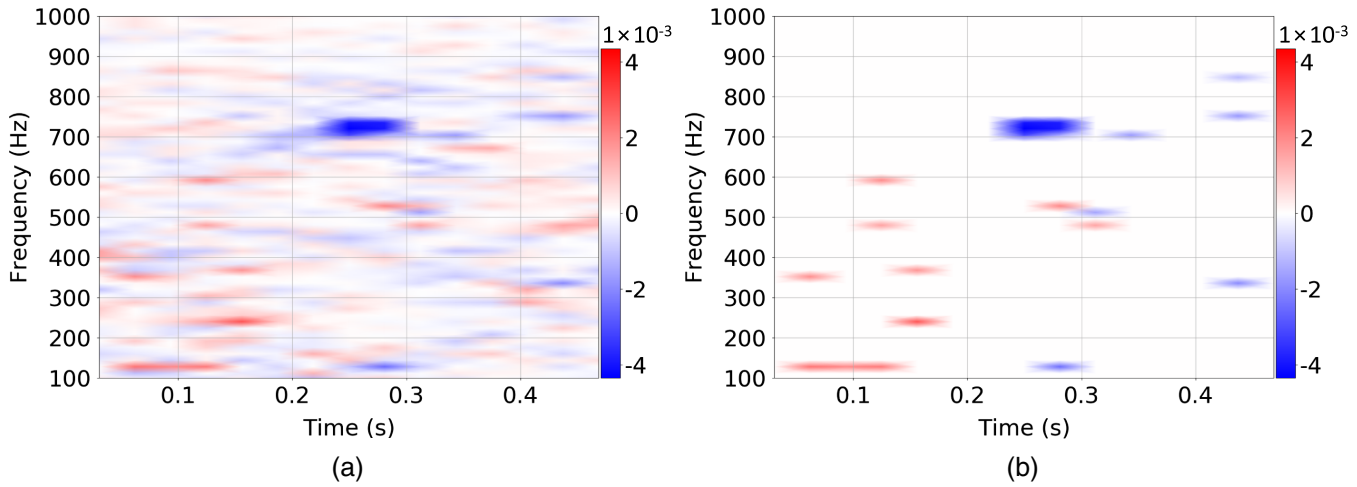

FIG. 4. The reconstruction of the V mode of a trigger where the injected waveform is SFHx. The upper panel shows the $\mathbf{V}_\mathrm{o}$ and the lower panel shows $\mathbf{V}_\mathrm{t}$ of the trigger. The source is located at (longitude, latitude) $= (-145°, 70°)$ and 10 kpc from Earth. The network of GW detectors consists of aLIGO Hanford, aLIGO Livingston, AdVirgo, and KAGRA.

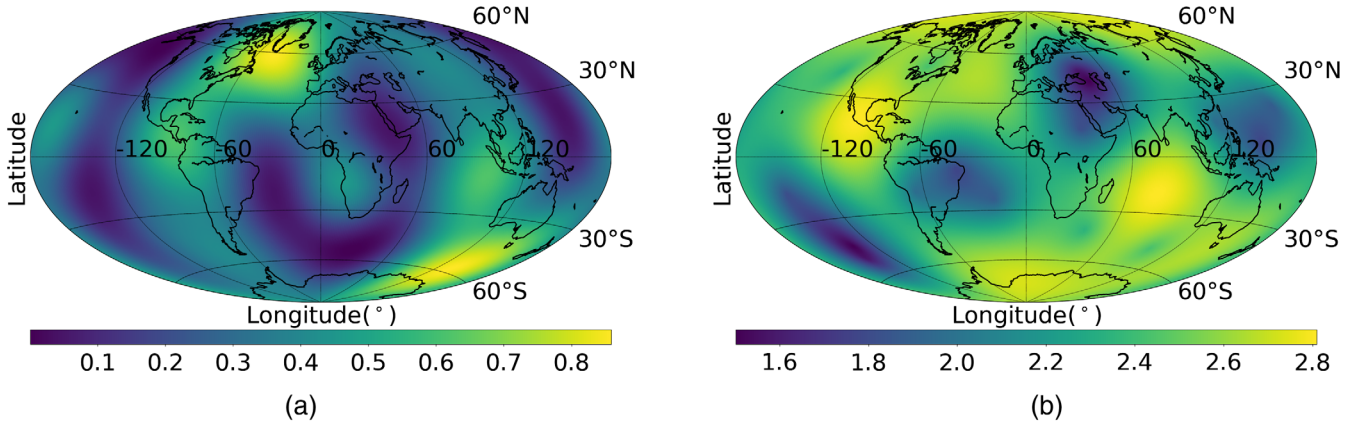

FIG. 5. The sky map on the left shows the distribution of the value of the denominator in Eq. (5) for a network of GW detectors consisted of aLIGO Hanford, aLIGO Livingston, AdVirgo, and KAGRA, while the sky map on the right shows the distribution of $A = \sqrt{\sum_j F_{j+}^2 + F_{j\times}^2}$ for the same network.

zero, the values on the right will approach infinity and become unphysical. This means, at such location, the two polarizations of GWs cannot be recovered. As an example, in Fig. 5(a), we show the distribution of this term across the sky for a network of GW detectors consisted of aLIGO Hanford, aLIGO Livingston, AdVirgo, and KAGRA. Clearly, even for a network of four detectors, there are still regions where the reconstruction of the two polarizations is not achievable. Shown in Fig. 5(b) is the value of $A = \sqrt{\sum_j F_{j+}^2 + F_{j\times}^2}$ for the network, where j indicates the jth detector. If such a value is large at a location, sources coming from this direction are more likely to be detectable to the network. As one may notice from these two plots, the patterns of the distributions do not completely coincide with each other. In particular, there are regions where one value is high but the other is low or vice versa. This means that it is possible the GWs from a source in the sky may be detectable, while the two polarizations and, thus, the V mode may not be recoverable. A question that can be raised, therefore, is, how observable will the V mode be if we have a detection of GWs from sources in the sky?

In this section, we try to answer this question by investigating how the values of $\log B_{\mathrm{H_1/H_0}}$ for a network of the four detectors are distributed. Again, the detectors are the aLIGO detectors, AdVirgo, and KAGRA. Specifically, we focus on CCSNe and employ the waveform referred to as SFHx in Ref. [48], shown in Fig. 6(a). The waveform was generated in a 3D full general relativity simulation of CCSN assuming a star of 15 $M_\odot$ at zero age. The simulation followed the hydrodynamics of the explosion from the beginning of the collapse for up to 300 ms after core bounce. The nuclear equation of state assumed was SFHx [54], which is currently considered the best-fit model

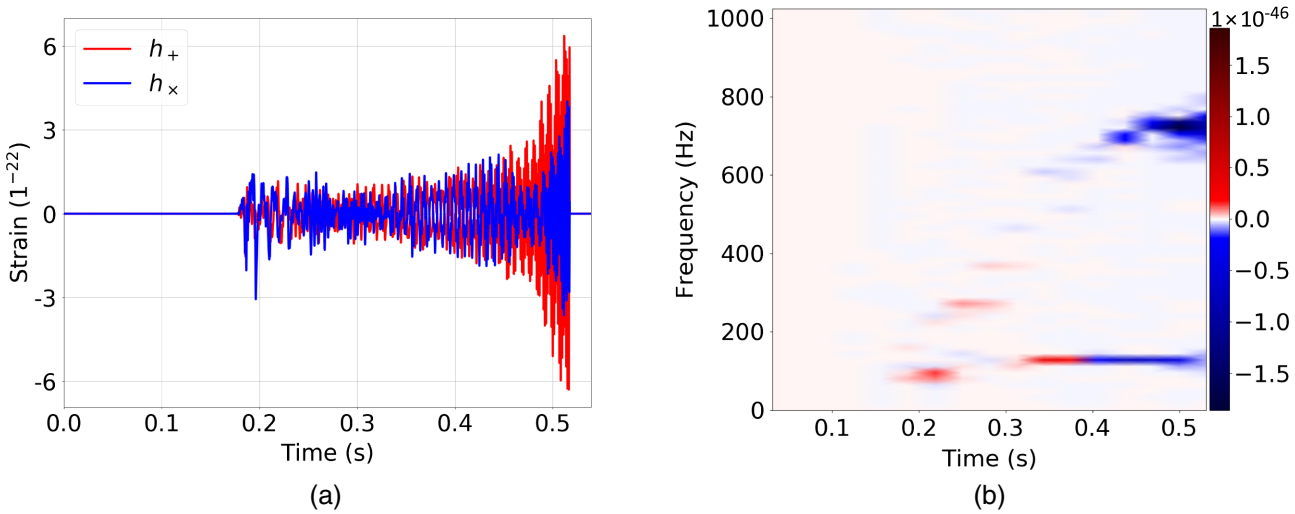

FIG. 6. Plots showing the waveform SFHx and its V mode. The left panel shows the waveform assuming a distance of 10 kpc from Earth. The right panel shows the V mode of the waveform at the same distance.

with the observed relation of mass radius of cold neutron stars [54,55]. The waveform is characterized by two distinct features, which are clearly reflected in its V mode shown in Fig. 6(b). The first is a power excess increasing from ∼100 to ∼800 Hz from after core bounce at ∼0.14 s. This feature is correlated with the oscillation of the proto-neutron-star surface [56]. This feature appears to occur stochastically in the V mode (the seemingly random change of the asymmetry between the right-handed and left-handed mode) due to buoyancy-driven proto-neutron-star surface oscillation, which also occurs stochastically [57]. In addition, a quasiperiodic modulation feature can be seen from 0.14 to 0.30 s at low frequency (∼100 Hz) caused by mass accretion flows, induced by the spiral motions of the SASI activities, striking the proto-neutron-star core surface. The feature is characterized by a dominance of right-handed mode from ∼0.14 to ∼0.20 s, which switches to a dominance of left-handed mode from ∼0.22 to ∼0.32 s. The strong and violent spiral SASI activity which leaves an imprint in its V mode is also one of the reasons that the waveform was chosen for this study. Between the dominance of different modes, a quiescent phase where the polarization of close to zero amplitude is observed.

For the purpose of investigating the detectability of the V mode for sources across the sky, we perform simulations at three different distances, i.e., 2, 5, and 10 kpc. For each

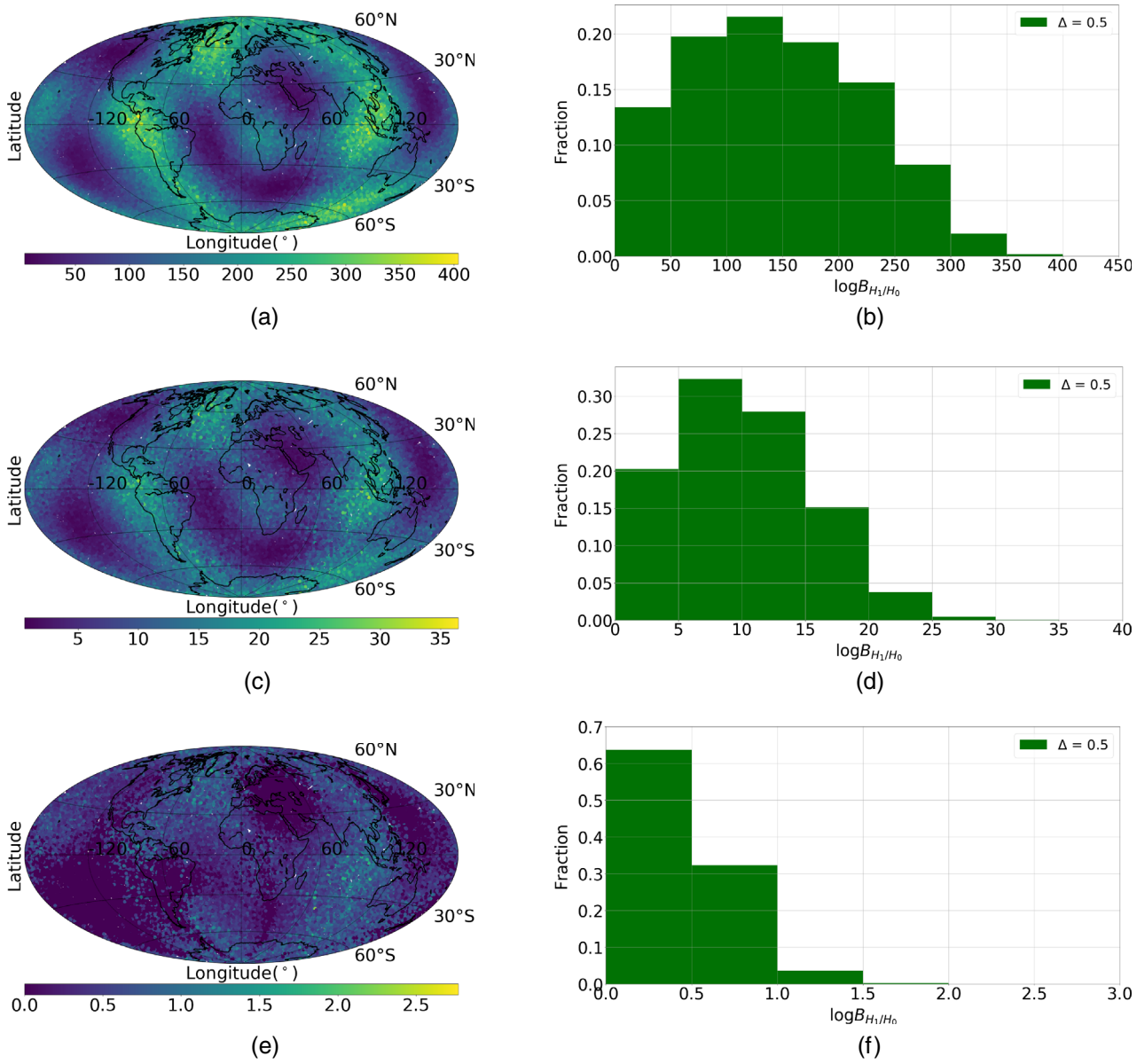

FIG. 7. The distributions of the values of log B_{H_1/H_0}. On the left, the sky maps show how the values of log B_{H_1/H_0} are distributed across the sky. On the right, the plots show the histogram of the values of log B_{H_1/H_0}. The value of Δ in the legends in the right panels are the bin size. From the top to the bottom, the distances are 2, 5, and 10 kpc, respectively.

TABLE I. Numerical results. From the left to the right, the first column is the distance for the sources, the second column means the fraction of injections that are detectable to cWB, and the third column indicates the fraction of the injections of which the values of $\log B_{\mathrm{H_1/H_0}}$ is no less than 8.

Distance	Detectable	$\log B_{\mathrm{H_1/H_0}} \geq 8$
2 kpc	100%	99.9%
5 kpc	100%	58.2%
10 kpc	69%	0.0%

distance, we generate 5×10^4 sources distributed in the sky assuming a uniform distribution on right ascension and on the sine of declination. When computing the value of $\log B_{\mathrm{H_1/H_0}}$ for an event, we choose N (the number of noise only whitened time series in the computation of the V mode) to be 2000 and F_o (the threshold for selecting pixels in the time-frequency domain) to be 0.99. For simplicity, we use simulated Gaussian noise generated using power spectrum densities of the detectors at their respective design sensitivities. Since we are focused on GWs from CCSNe, we assume that information on the sky locations of the sources and the arrival times of the signals are available from electromagnetic and/or neutrino observations. This means when recovering the V mode of a trigger, we use the true values of the $\mathbf{F}_+$ and $\mathbf{F}_\times$ as well as the arrival times.

V. DISCUSSION

A. SFHx

We present the results of the simulations in this section. Specifically, the results for 2, 5, and 10 kpc are shown in

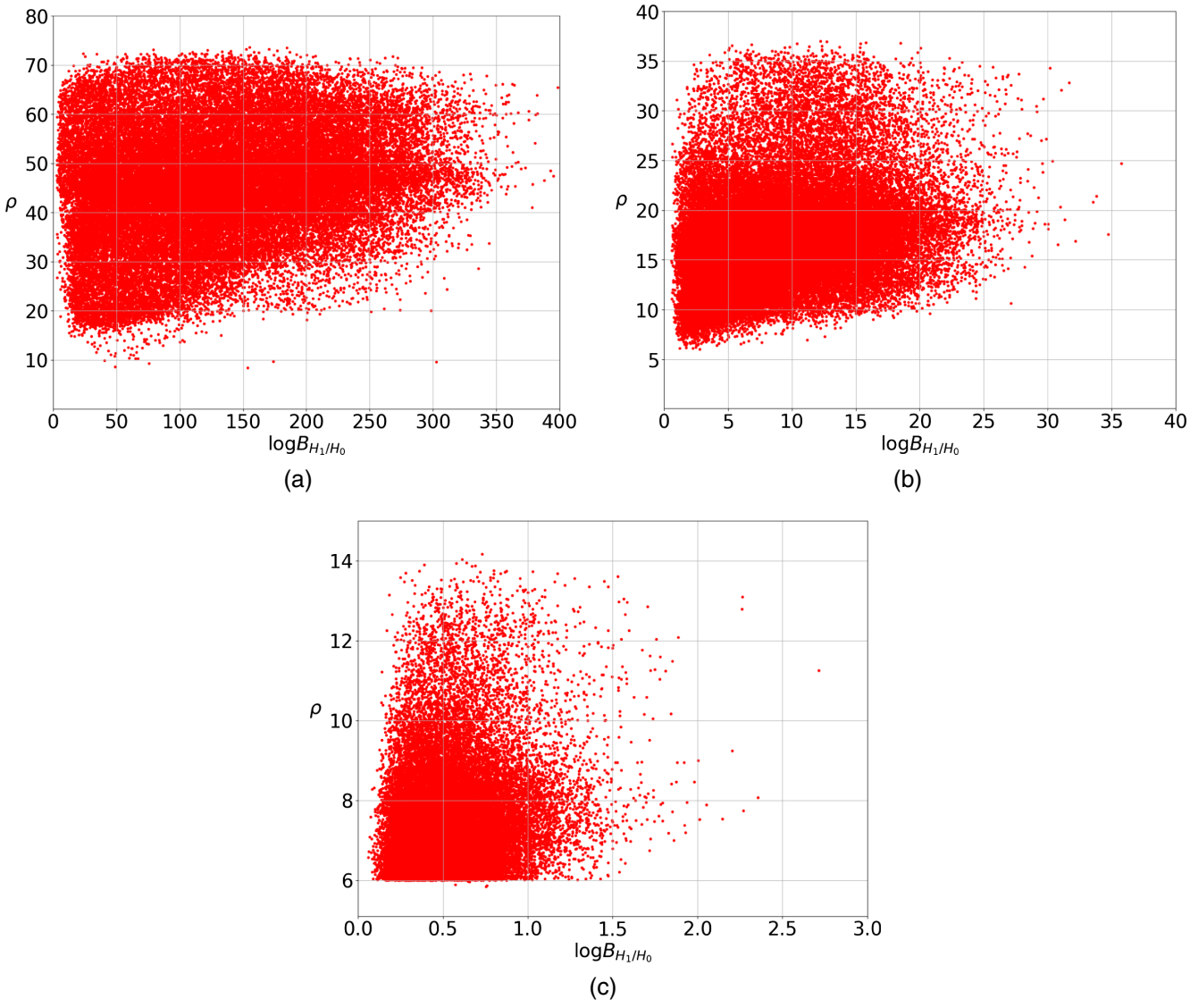

FIG. 8. Plots showing the values of ρ (see the text for definition) as a function of $\log B_{\mathrm{H_1/H_0}}$. From the top to the bottom, the sources are at 2, 5, and 10 kpc, respectively.

Fig. 7. It can be seen that there are sky regions where the values of $\log B_{H_1/H_0}$ are higher than that at the other regions. In particular, for sources at 2 kpc, the distribution of $\log B_{H_1/H_0}$ forms a pattern that is consistent with the pattern shown in Fig. 5(a). This is somewhat expected, since the V mode relies on the reconstruction of the two polarizations of GWs. However, it is noticeable that regions where the values are the highest in Fig. 5(a) are not the highest in Fig. 7(a) [for example, one of the highest values in Fig. 5(a) occurs at $(\text{longitude}, \text{latitude}) = (\sim 60°, \sim 60°)$, while the largest Bayes factor for sources at 2 kpc happens at $(\text{longitude}, \text{latitude}) = (\sim -100°, \sim 0°)$]. That is because the amplitudes of the signal are first modulated by the antenna pattern of the detector networks. This means the distribution of $\log B_{H_1/H_0}$ is affected by not only the denominator of the term on the right-hand side in Eq. (5), but also the combined antenna pattern of the network of GW detectors. For sources at 5 kpc, the same pattern appears with lower values of $\log B_{H_1/H_0}$, as the amplitudes of the signals are inversely proportional to the distance. The distributions of $\log B_{H_1/H_0}$ for sources at these distances are shown in the right panels in Fig. 7. If a value of $\log B_{H_1/H_0} \geq 8$ is required to claim a detection of the V mode, that would be 99.9% and 58.2% of the injections for 2 and 5 kpc, respectively.

However, for sources at 10 kpc, the distribution in the sky map appears to be different. As stated in Sec. III, the SCP algorithm will be called only when a trigger is identified by the pipeline cWB. For closer distances such as 5 and 2 kpc, this may not appear to be a problem, as the majority of the sources are detectable with the cWB. But for 10 kpc, a noticeable fraction of the sources start to be undetectable, resulting in a different distribution of $\log B_{H_1/H_0}$. Further, if we again employ the same criterion for $\log B_{H_1/H_0}$ (i.e., $\log B_{H_1/H_0} \geq 8$), that would mean at 10 kpc no V mode is detectable. We present the fraction of detectable sources and the fraction of sources with $\log B_{H_1/H_0} \geq 8$ in Table I.

From the results above, it can be seen that there is a relation between the detectability of a signal and that of its V mode. To show this, we present our results from another perspective. We plot the values of ρ as a function of $\log B_{H_1/H_0}$, where ρ is defined by the following equation:

$$\rho = \sqrt{\frac{E_c}{J - 1}}, \tag{10}$$

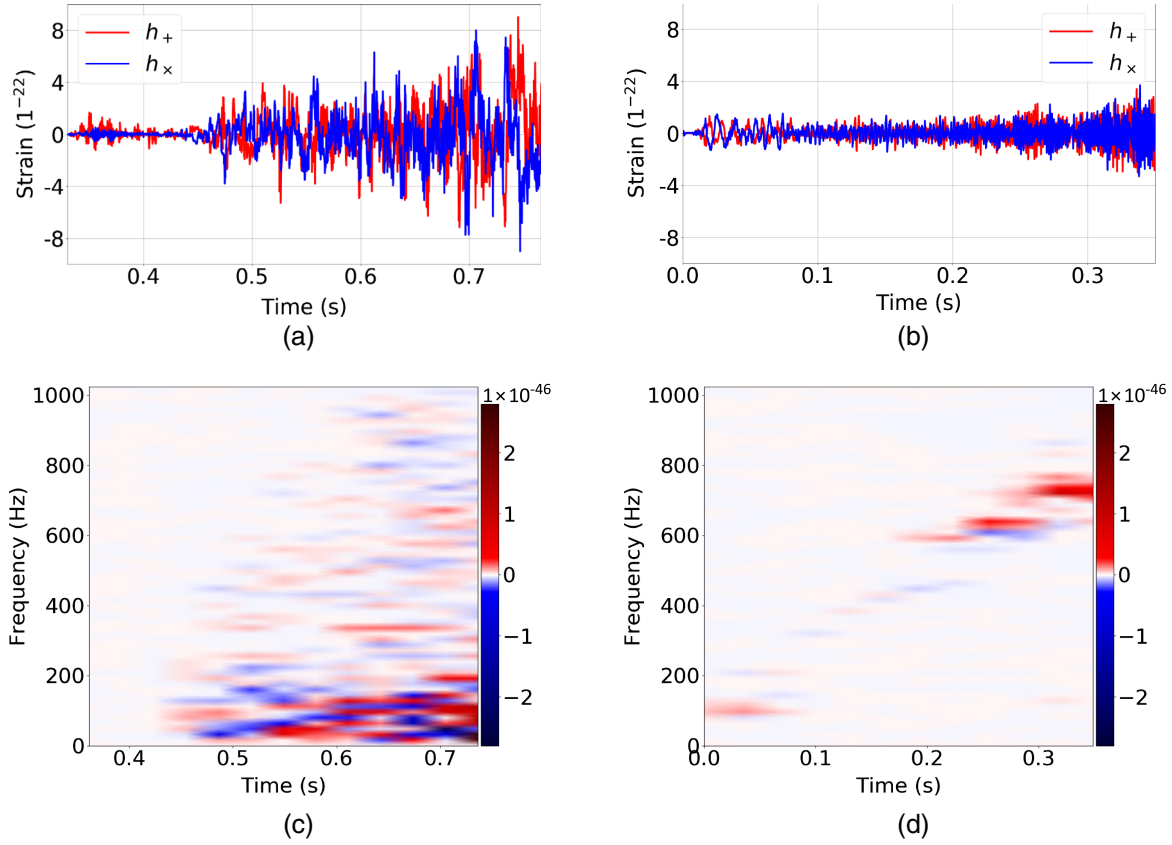

FIG. 9. Simulated supernova waveforms and their V modes. The top left panel shows a waveform from Ref. [59], assuming an equatorial observer and a nonrotating progenitor of 12 $M_\odot$. The top right panel shows a waveform from Ref. [48], where the progenitor is 15 $M_\odot$ with zero rotation and a polar observer is assumed. For both waveforms, the sources are assumed to be at a distance of 10 kpc from Earth. The lower panels show the corresponding V modes. For all panels, the x axes show the time after core bounce.

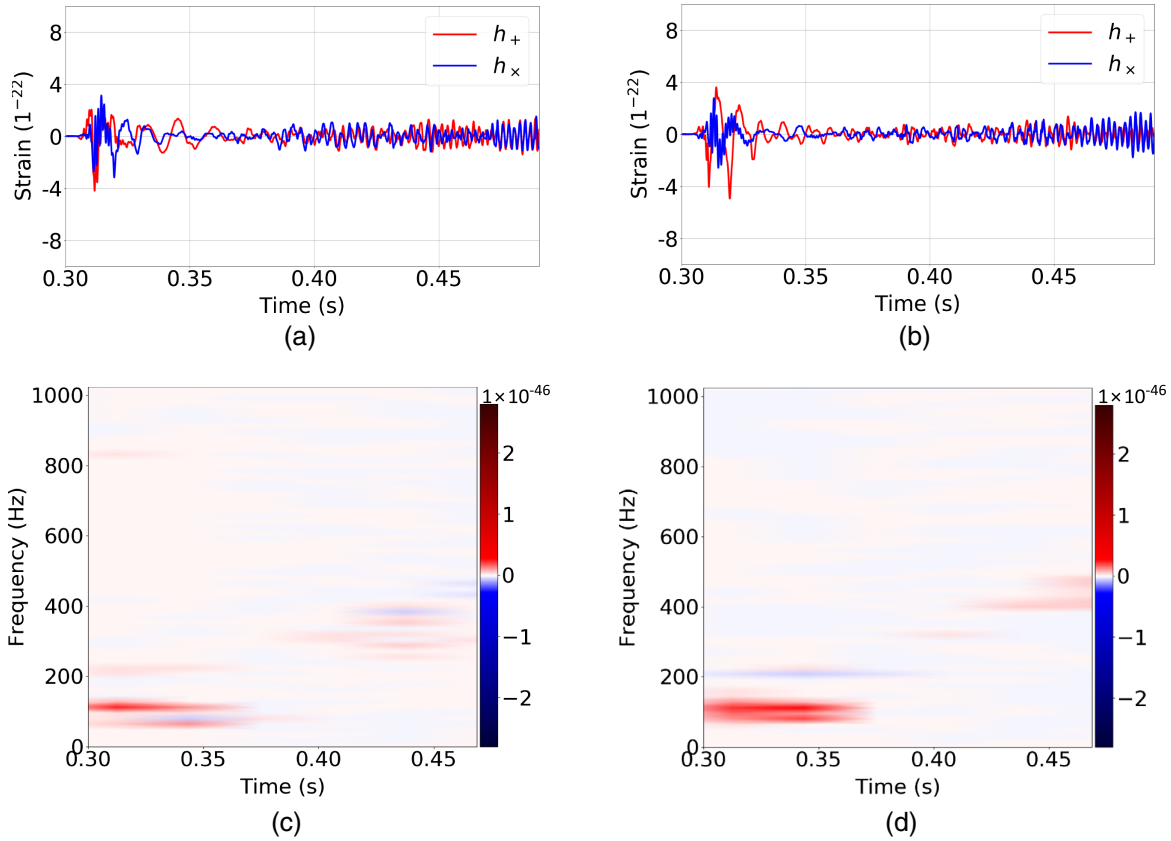

FIG. 10. Simulated supernova waveforms and their V modes. The waveforms in the tops panels are taken from Ref. [60]. The progenitors are 27 $M_\odot$. The waveform shown in the top left panel assumes an equatorial observer, while the one on the right a polar observer. For both waveforms, the sources are assumed to be at a distance of 10 kpc from Earth. The lower panels show the corresponding V modes. For all panels, the x axes show the time after core bounce.

where J is the number of detectors in a network and E_c is referred to as the coherent energy and is defined in Ref. [58]. The value of ρ is one of the most important criteria based on which cWB determines if a trigger is identified in the data. In Fig. 8(c), a low cutoff of $\rho = 6$ can be seen. This is caused by the minimal value of ρ required for a trigger. Interestingly, for $\log B_{H_1/H_0} > 1.5$, the lowest value of ρ seems to change linearly. This proves that the values of $\log B_{H_1/H_0}$ partially depends on the detectability of a signal.

It is also worth noting that the sources in this simulation were injected with $\iota = 0°$, which would maximize the V mode detectability. This limitation was due to the fact that the SFHx was available at only one observing angle. In reality, since any inclination angle would be equally likely, it can be expected the distribution of $\log B_{H_1/H_0}$ will be shifted toward smaller values.

As stated before, the SCP algorithm will be called to compute the V mode of a signal only if the signal is detectable to cWB. This requirement has the advantage of increasing the confidence in the event of a detection. However, it is possible that such a requirement can potentially cause signals to be overlooked that may otherwise be detectable, because the detectability of V modes may not be completely correlated with the detectability of the signals using more traditional methods as shown in Ref. [38]. For future study, to circumvent this problem, we plan to relax such a requirement by expanding the SCP algorithm and employing only the V mode as detection statistics.

B. Waveform comparison

To provide broader context to the results presented above, in this section, we use various simulated supernova waveforms as injections and employ the SCP algorithm to estimate the detectability and the strength of their V modes. The waveforms are chosen from Refs. [47,48,59–61] such that the strength of the V modes will range from strong to weak. The waveforms are shown below in Figs. 9–11 and their details given in Table II. The waveforms will be referred to using the names shown in the first column. Among all the selected waveforms, in terms of its V mode, Yak and SFHx have the strongest V modes. $An2^P$, Ott^E, and Ott^P have weak to medium V modes compared to the rest of the waveforms, while An1 and $An2^E$ are almost completely linearly polarized and, thus, have no obvious V

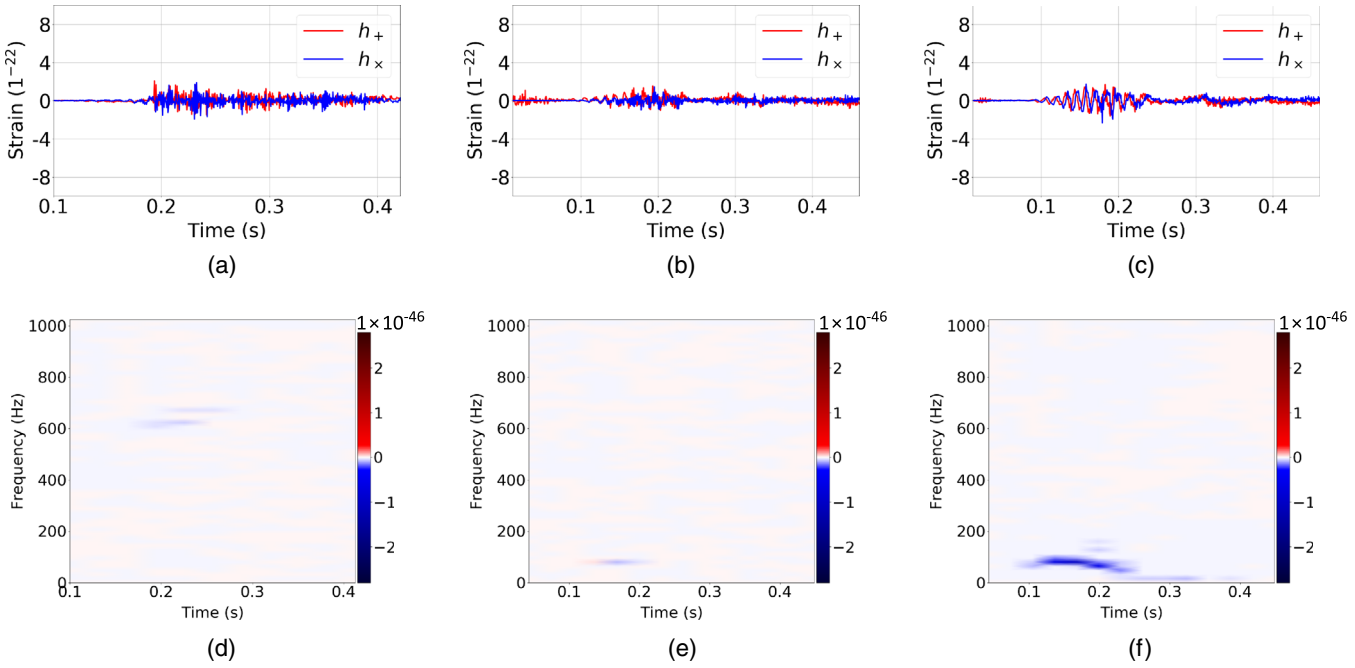

FIG. 11. Simulated supernova waveforms and their V modes. The top left panel shows a waveform from Ref. [47], assuming an equatorial observer and a nonrotating progenitor of 20 $M_\odot$. The top middle right panels show two waveforms from Ref. [61], where the progenitors are 15 $M_\odot$ with rotating profiles labeled as fr (fast rotating) in Ref. [61]. The top middle panel assumes an equatorial observer while the top right one a polar observer. For all waveforms, the sources are assumed to be at a distance of 10 kpc from Earth. The lower panels show the corresponding V modes. For all panels, the x axes show the time after core bounce.

modes. For simplicity but without loss of generality, a sky location is randomly chosen to be $(\text{longitude}, \text{latitude}) = (-81.2°, 43.3°)$ for injections. For each waveform, 100 sources are injected at the said sky location. Since we are more interested in the relative strength between the V modes of the waveforms rather than the detectability of the waveforms to cWB, the distance from Earth to the sources is deliberately chosen to be close at 2 kpc, so that the waveforms will be detectable to cWB. The results are shown in Fig. 12. For each waveform, we present the value of $\log B_{\mathrm{H_1/H_0}}$ averaged over the 100 sources. It can be seen that the V modes of An1 and An2$^{\mathrm{E}}$ are not detectable, which is not surprising, because as mentioned these waveforms are linearly polarized. The values of $\log B_{\mathrm{H_1/H_0}}$ for other waveforms are observed to be consistent with the V modes shown in Figs. 9–11. Figure 12 seems to suggest that strong V modes are not a prevalent feature of supernova waveforms; however, it should be pointed out that, although this may be the case, only a small set of the simulated waveforms currently existing in the

TABLE II. Waveforms. From the left to the right, the first column is the names for the waveforms, the second column shows the masses of the progenitors, and the third column indicates the observing angles at which the waveforms are extracted.

Name	Mass ($M_\odot$)	Observing angle
Yak [59]	15	Equatorial
TM1 [48]	15	Polar
Ott$^{\mathrm{E}}$ [60]	27	Equatorial
Ott$^{\mathrm{P}}$ [60]	27	Polar
An1 [47]	20	Equatorial
An2$^{\mathrm{E}}$ [61]	15	Equatorial
An2$^{\mathrm{P}}$ [61]	15	Polar

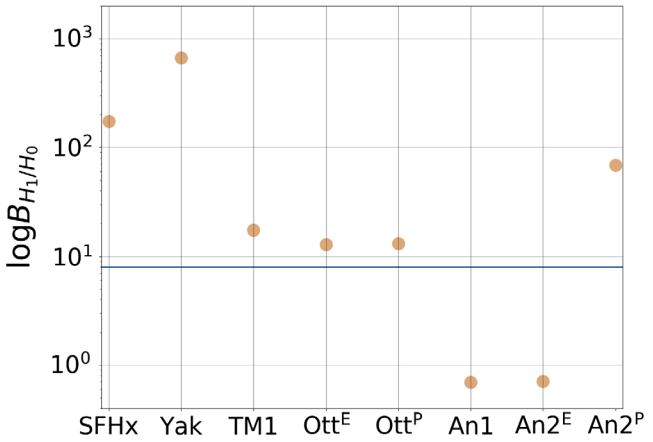

FIG. 12. The values of $\log B_{\mathrm{H_1/H_0}}$ for the waveforms, averaged over 100 injections at $(\text{longitude}, \text{latitude}) = (-81.2°, 43.3°)$, 2 kpc from Earth. The solid line at $\log B_{\mathrm{H_1/H_0}} = 8$ shows the minimum requirement for a detection of V mode to be deemed significant.

literature were studied. A more thorough study with more supernova waveforms will be carried out in a future study.

We argue that, although simulations where the sources are randomly distributed across the sky presented in this paper is done using only one waveform (i.e., SFHx), the applicability of the results is not limited. In fact, the results can be extrapolated to other waveforms by comparing the V mode of other waveforms with the V mode of the SFHx waveform shown in Fig. 6 and the values of $\log B_{\mathrm{H_1/H_0}}$ of their V mode using the method laid out in Sec. III as was done in this section.

VI. CONCLUSION

We have developed an algorithm referred to as the SCP algorithm that works with the pipeline cWB. Using the whitened time series from the cWB as well as the estimates of the sky locations and the arrival times of events or those from electromagnetic and/or neutrino observations, the algorithm will recover the V mode if a trigger is identified by the cWB. The Bayes factor is employed to determine whether a V mode signature is significant.

By using the SFHx waveform as an example and simulating 5×10^4 sources for three different distances, we investigated the distribution of $\log B_{\mathrm{H_1/H_0}}$ for sources across the sky with a network of four GW detectors. We showed that, for sources at 2 and 5 kpc, the distributions of $\log B_{\mathrm{H_1/H_0}}$ are consistent with how regions are distributed where the two polarizations of GWs are recoverable. The values of $\log B_{\mathrm{H_1/H_0}}$, however, will be partially dependent on the combined antenna pattern of the network. The distribution of $\log B_{\mathrm{H_1/H_0}}$ for sources at 10 kpc appears to be different, as the sources are starting to be undetectable. Using a criterion of $\log B_{\mathrm{H_1/H_0}} \geq 8$ for a detection of the V mode, we showed that, for waveform SFHx, 99.9% and 58.2% of the V mode of sources at 2 and 5 kpc, respectively, are detectable, while for sources at 10 kpc, no V mode is detectable.

We have conducted a simple analysis where we compared the V modes of different waveforms and showed that the results shown in this work can be extrapolated to other waveform morphologies. This can be done by comparing the waveforms of interest to the SFHx waveform shown in this paper.

ACKNOWLEDGMENTS

This work is partially supported by JSPS KAKENHI Grants No. JP19K03896 and No. JP17H06364. We express our gratitude to Marek Szczepanczyk and Sergey Klimenko for the helpful discussions of this work. We are also thankful to Kanda Nobuyuki, Kei Kotake, Takiwaki Tomoya, Chris Messenger, and Ik Siong Heng, for their constructive comments. We are grateful to the anonymous reviewer for their thorough and constructive comments on the paper.

[1] B. P. Abbott, R. Abbott, T. D. Abbott, M. R. Abernathy, F. Acernese, K. Ackley, C. Adams, T. Adams, P. Addesso, R. X. Adhikari *et al.*, Observation of Gravitational Waves from a Binary Black Hole Merger, Phys. Rev. Lett. **116**, 061102 (2016).

[2] B. P. Abbott, R. Abbott, T. D. Abbott, M. R. Abernathy, F. Acernese, K. Ackley, C. Adams, T. Adams, P. Addesso, R. X. Adhikari *et al.*, Gw151226: Observation of Gravitational Waves from a 22-Solar-Mass Binary Black Hole Coalescence, Phys. Rev. Lett. **116**, 241103 (2016).

[3] B. P. Abbott, R. Abbott, T. D. Abbott, F. Acernese, K. Ackley, C. Adams, T. Adams, P. Addesso, R. X. Adhikari, V. B. Adya *et al.*, GW170608: Observation of a 19 solar-mass binary black hole coalescence, Astrophys. J. Lett. **851**, L35 (2017).

[4] B. P. Abbott, R. Abbott, T. D. Abbott, F. Acernese, K. Ackley, C. Adams, T. Adams, P. Addesso, R. X. Adhikari, V. B. Adya *et al.*, GW170814: A Three-Detector Observation of Gravitational Waves from a Binary Black Hole Coalescence, Phys. Rev. Lett. **119**, 141101 (2017).

[5] B. P. Abbott, R. Abbott, T. D. Abbott, F. Acernese, K. Ackley, C. Adams, T. Adams, P. Addesso, R. X. Adhikari, V. B. Adya *et al.*, PGW170817: Observation of Gravitational Waves from a Binary Neutron Star Inspiral, Phys. Rev. Lett. **119**, 161101 (2017).

[6] B. P. Abbott, R. Abbott, T. D. Abbott, F. Acernese, K. Ackley, C. Adams, T. Adams, P. Addesso, R. X. Adhikari, V. B. Adya *et al.*, Gravitational waves and gamma-rays from a binary neutron star merger: GW170817 and GRB 170817A, Astrophys. J. Lett. **848**, L13 (2017).

[7] B. P. Abbott, R. Abbott, T. D. Abbott, F. Acernese, K. Ackley, C. Adams, T. Adams, P. Addesso, R. X. Adhikari, V. B. Adya *et al.*, Multi-messenger observations of a binary neutron star merger, Astrophys. J. Lett. **848**, L12 (2017).

[8] B. P. Abbott, R. Abbott, T. D. Abbott, S. Abraham, F. Acernese, K. Ackley, C. Adams, R. X. Adhikari, V. B. Adya, C. Affeldt *et al.*, GWTC-1: A Gravitational-Wave Transient Catalog of Compact Binary Mergers Observed by Ligo and Virgo During the First and Second Observing Runs, Phys. Rev. X **9**, 031040 (2019).

[9] B. P. Abbott, R. Abbott, T. D. Abbott, M. R. Abernathy, F. Acernese, K. Ackley, C. Adams, T. Adams, P. Addesso, R. X. Adhikari *et al.*, Prospects for observing and localizing gravitational-wave transients with Advanced Ligo,

Advanced Virgo and KAGRA, Living Rev. Relativity **21**, 3 (2018).
[10] J. Aasi, B. P. Abbott, R. Abbott, T. Abbott, M. R. Abernathy, K. Ackley, C. Adams, T. Adams, P. Addesso, R. X. Adhikari *et al.*, Advanced Ligo, Classical Quantum Gravity **32**, 074001 (2015).
[11] F. Acernese, M. Agathos, K. Agatsuma, D. Aisa, N. Allemandou, A. Allocca, J. Amarni, P. Astone, G. Balestri, G. Ballardin *et al.*, Advanced Virgo: A second-generation interferometric gravitational wave detector, Classical Quantum Gravity **32**, 024001 (2015).
[12] Y. Aso, Y. Michimura, K. Somiya, M. Ando, O. Miyakawa, T. Sekiguchi, D. Tatsumi, H. Yamamoto *et al.* (KAGRA Collaboration), Interferometer design of the KAGRA gravitational wave detector, Phys. Rev. D **88**, 043007 (2013).
[13] S. E. Gossan, P. Sutton, A. Stuver, M. Zanolin, K. Gill, and C. D. Ott, Observing gravitational waves from core-collapse supernovae in the advanced detector era, Phys. Rev. D **93**, 042002 (2016).
[14] B. P. Abbott, R. Abbott, T. D. Abbott, M. R. Abernathy, F. Acernese, K. Ackley, C. Adams, T. Adams, P. Addesso, R. X. Adhikari *et al.*, First targeted search for gravitational-wave bursts from core-collapse supernovae in data of first-generation laser interferometer detectors, Phys. Rev. D **94**, 102001 (2016).
[15] E. Baron and J. Cooperstein, The effect of iron core structure on supernovae, Astrophys. J. **353**, 597 (1990).
[16] H. A. Bethe, Supernova mechanisms, Rev. Mod. Phys. **62**, 801 (1990).
[17] E. O'Connor and C. D. Ott, Black hole formation in failing core-collapse supernovae, Astrophys. J. **730**, 70 (2011).
[18] K. Sato and H. Suzuki, Analysis of Neutrino Burst from the Supernova 1987A in the Large Magellanic Cloud, Phys. Rev. Lett. **58**, 2722 (1987).
[19] H.-T. Janka, Explosion mechanisms of core-collapse supernovae, Annu. Rev. Nucl. Part. Sci. **62**, 407 (2012).
[20] H. A. Bethe and J. R. Wilson, Revival of a stalled supernova shock by neutrino heating, Astrophys. J. **295**, 14 (1985).
[21] J. M. LeBlanc and J. R. Wilson, A numerical example of the collapse of a rotating magnetized star, Astrophys. J. **161**, 541 (1970).
[22] A. Burrows, L. Dessart, E. Livne, C. D. Ott, and J. Murphy, Simulations of magnetically driven supernova and hypernova explosions in the context of rapid rotation, Astrophys. J. **664**, 416 (2007).
[23] T. Takiwaki, K. Kotake, and K. Sato, Special relativistic simulations of magnetically dominated jets in collapsing massive stars, Astrophys. J. **691**, 1360 (2009).
[24] S. G. Moiseenko, G. S. Bisnovatyi-Kogan, and N. V. Ardeljan, A magnetorotational core-collapse model with jets, Mon. Not. R. Astron. Soc. **370**, 501 (2006).
[25] P. Mösta, S. Richers, C. D. Ott, R. Haas, A. L. Piro, K. Boydstun, E. Abdikamalov, C. Reisswig, and E. Schnetter, Magnetorotational core-collapse supernovae in three dimensions, Astrophys. J. Lett. **785**, L29 (2014).
[26] M. Obergaulinger and M. Á. Aloy, Magnetorotational core collapse of possible GRB progenitors. I. explosion mechanisms, Mon. Not. R. Astron. Soc. **492**, 4613 (2020).
[27] S. E. Woosley and A. Heger, The progenitor stars of gamma-ray bursts, Astrophys. J. **637**, 914 (2006).
[28] S.-C. Yoon and N. Langer, On the evolution of rapidly rotating massive white dwarfs towards supernovae or collapses, Astron. Astrophys. **435**, 967 (2005).
[29] S. E. De Mink, N. Langer, R. G. Izzard, H. Sana, and A. de Koter, The rotation rates of massive stars: The role of binary interaction through tides, mass transfer, and mergers, Astrophys. J. **764**, 166 (2013).
[30] M. Obergaulinger and M. Á. Aloy, Protomagnetar and black hole formation in high-mass stars, Mon. Not. R. Astron. Soc. **469**, L43 (2017).
[31] J. M. Blondin, A. Mezzacappa, and C. DeMarino, Stability of standing accretion shocks, with an eye toward core-collapse supernovae, Astrophys. J. **584**, 971 (2003).
[32] N. Langer, Presupernova evolution of massive single and binary stars, Annu. Rev. Astron. Astrophys. **50**, 107 (2012).
[33] O. H. Ramírez-Agudelo, H. Sana, A. de Koter, S. Simón-Díaz, S. E. de Mink, F. Tramper, P. L. Dufton, C. J. Evans, G. Gräfener, A. Herrero *et al.*, Rotational velocities of single and binary o-type stars in the tarantula nebula, Proc. Int. Astron. Union **9**, 76 (2014).
[34] A. Maeder and G. Meynet, Rotating massive stars: From first stars to gamma ray bursts, Rev. Mod. Phys. **84**, 25 (2012).
[35] K. Hayama, S. Desai, K. Kotake, S. D. Mohanty, M. Rakhmanov, T. Summerscales, and S. Yoshida, Determination of the angular momentum distribution of supernovae from gravitational wave observations, Classical Quantum Gravity **25**, 184022 (2008).
[36] E. Abdikamalov, S. Gossan, A. M. DeMaio, and C. D. Ott, Measuring the angular momentum distribution in core-collapse supernova progenitors with gravitational waves, Phys. Rev. D **90**, 044001 (2014).
[37] K. Hayama, T. Kuroda, K. Nakamura, and S. Yamada, Circular Polarizations of Gravitational Waves from Core-Collapse Supernovae: A Clear Indication of Rapid Rotation, Phys. Rev. Lett. **116**, 151102 (2016).
[38] K. Hayama, T. Kuroda, K. Kotake, and T. Takiwaki, Circular polarization of gravitational waves from non-rotating supernova cores: A new probe into the pre-explosion hydrodynamics, Mon. Not. R. Astron. Soc. **477**, L96 (2018).
[39] T. Kuroda, T. Takiwaki, and K. Kotake, Gravitational wave signatures from low-mode spiral instabilities in rapidly rotating supernova cores, Phys. Rev. D **89**, 044011 (2014).
[40] N. Seto and A. Taruya, Measuring a Parity-Violation Signature in the Early Universe via Ground-Based Laser Interferometers, Phys. Rev. Lett. **99**, 121101 (2007).
[41] S. van den Bergh and G. A. Tammann, Galactic and extragalactic supernova rates, Annu. Rev. Astron. Astrophys. **29**, 363 (1991).
[42] E. Cappellaro, M. Turatto, D. Yu. Tsvetkov, O. S. Bartunov, I. N. Makarova *et al.*, The rate of supernovae. II. The selection effects and the frequencies per unit blue luminosity, arXiv:astro-ph/9302017.
[43] B. C. Reed, New estimates of the solar-neighborhood massive star birthrate and the galactic supernova rate, Astron. J. **130**, 1652 (2005).

[44] S. W. Bruenn, E. J. Lentz, W. R. Hix, A. Mezzacappa, J. A. Harris, O. E. B. Messer, E. Endeve, J. M. Blondin, M. A. Chertkow, E. J. Lingerfelt *et al.*, The development of explosions in axisymmetric ab initio core-collapse supernova simulations of 12–25 stars, Astrophys. J. **818**, 123 (2016).

[45] A. Heger, S. E. Woosley, and H. C. Spruit, Presupernova evolution of differentially rotating massive stars including magnetic fields, Astrophys. J. **626**, 350 (2005).

[46] T. Takiwaki, K. Kotake, and Y. Suwa, Three-dimensional simulations of rapidly rotating core-collapse supernovae: Finding a neutrino-powered explosion aided by non-axisymmetric flows, Mon. Not. R. Astron. Soc. **461**, L112 (2016).

[47] H. Andresen, B. Müller, E. Müller, and H.-T. Janka, Gravitational wave signals from 3d neutrino hydrodynamics simulations of core-collapse supernovae, Mon. Not. R. Astron. Soc. **468**, 2032 (2017).

[48] T. Kuroda, K. Kotake, and T. Takiwaki, A new gravitational-wave signature from standing accretion shock instability in supernovae, Astrophys. J. Lett. **829**, L14 (2016).

[49] S. Klimenko, G. Vedovato, M. Drago, F. Salemi, V. Tiwari, G. A. Prodi, C. Lazzaro, K. Ackley, S. Tiwari, C. F. Da Silva, and G. Mitselmakher, Method for detection and reconstruction of gravitational wave transients with networks of advanced detectors, Phys. Rev. D **93**, 042004 (2016).

[50] B. P. Abbott, R. Abbott, T. D. Abbott, M. R. Abernathy, F. Acernese, K. Ackley, C. Adams, T. Adams, P. Addesso, R. X. Adhikari *et al.*, Observing gravitational-wave transient GW150914 with minimal assumptions, Phys. Rev. D **93**, 122004 (2016).

[51] H. Kawahara, T. Kuroda, T. Takiwaki, K. Hayama, and K. Kotake, A linear and quadratic time–frequency analysis of gravitational waves from core-collapse supernovae, Astrophys. J. **867**, 126 (2018).

[52] I. Di Palma and M. Drago, Estimation of the gravitational wave polarizations from a nontemplate search, Phys. Rev. D **97**, 023011 (2018).

[53] T. Akutsu, M. Ando, K. Arai, Y. Arai, S. Araki, A. Araya, N. Aritomi, H. Asada, Y. Aso, S. Atsuta *et al.*, Kagra: 2.5 generation interferometric gravitational wave detector, Nat. Astron. **3**, 35 (2019).

[54] A. W. Steiner, M. Hempel, and T. Fischer, Core-collapse supernova equations of state based on neutron star observations, Astrophys. J. **774**, 17 (2013).

[55] A. W. Steiner, J. M. Lattimer, and E. F. Brown, The equation of state from observed masses and radii of neutron stars, Astrophys. J. **722**, 33 (2010).

[56] B. Müller, H.-T. Janka, and A. Marek, A new multi-dimensional general relativistic neutrino hydrodynamics code of core-collapse supernovae. III. Gravitational wave signals from supernova explosion models, Astrophys. J. **766**, 43 (2013).

[57] J. W. Murphy, C. D. Ott, and A. Burrows, A model for gravitational wave emission from neutrino-driven core-collapse supernovae, Astrophys. J. **707**, 1173 (2009).

[58] S. Klimenko, G. Vedovato, M. Drago, F. Salemi, V. Tiwari, G. A. Prodi, C Lazzaro, K. Ackley, S. Tiwari, C. F. Da Silva *et al.*, Method for detection and reconstruction of gravitational wave transients with networks of advanced detectors, Phys. Rev. D **93**, 042004 (2016).

[59] K. N. Yakunin, A. Mezzacappa, P. Marronetti, E. J. Lentz, S. W. Bruenn, W. R. Hix, O. E. Messer, E. Endeve, J. M. Blondin, and J. A. Harris, The gravitational wave signal of a core collapse supernova explosion of a 15 $M_{\odot}$ star, arXiv: 1701.07325.

[60] C. D. Ott, E. Abdikamalov, P. Mösta, R. Haas, S. Drasco, E. P. O'Connor, C. Reisswig, C. A. Meakin, and E. Schnetter, General-relativistic simulations of three-dimensional core-collapse supernovae, Astrophys. J. **768**, 115 (2013).

[61] H. Andresen, E. Mller, H.-T. Janka, A. Summa, K. Gill, and M. Zanolin, Gravitational waves from 3D core-collapse supernova models: The impact of moderate progenitor rotation, Mon. Not. R. Astron. Soc. **486**, 2238 (2019).